PUBLICATIONS OF THE ASTRONOMICAL SOCIETY OF THE PACIFIC, **119**: 1038–1051, 2007 September

Absolute Calibration and Characterization of the Multiband Imaging Photometer for *Spitzer*. III. An Asteroid-based Calibration of MIPS at 160 μm

J. A. STANSBERRY,[1] K. D. GORDON,[1] B. BHATTACHARYA,[2] C. W. ENGELBRACHT,[1] G. H. RIEKE,[1] F. R. MARLEAU,[2] D. FADDA,[2] D. T. FRAYER,[2] A. NORIEGA-CRESPO,[2] S. WACHTER,[2] E. T. YOUNG,[1] T. G. MÜLLER,[3] D. M. KELLY,[1] M. BLAYLOCK,[1] D. HENDERSON,[2] G. NEUGEBAUER,[1] J. W. BEEMAN,[4] AND E. E. HALLER[4,5]
Received 2006 November 15; accepted 2007 July 25; published 2007 September 28

ABSTRACT. We describe the absolute calibration of the Multiband Imaging Photometer for *Spitzer* (MIPS) 160 μm channel. After the on-orbit discovery of a near-IR ghost image that dominates the signal for sources hotter than about 2000 K, we adopted a strategy utilizing asteroids to transfer the absolute calibrations of the MIPS 24 and 70 μm channels to the 160 μm channel. Near-simultaneous observations at all three wavelengths are taken, and photometry at the two shorter wavelengths is fit using the standard thermal model. The 160 μm flux density is predicted from those fits and compared with the observed 160 μm signal to derive the conversion from instrumental units to surface brightness. The calibration factor we derive is 41.7 MJy sr^{-1} $MIPS160^{-1}$ (MIPS160 being the instrumental units). The scatter in the individual measurements of the calibration factor, as well as an assessment of the external uncertainties inherent in the calibration, lead us to adopt an uncertainty of 5.0 MJy sr^{-1} $MIPS160^{-1}$ (12%) for the absolute uncertainty on the 160 μm flux density of a particular source as determined from a single measurement. For sources brighter than about 2 Jy, nonlinearity in the response of the 160 μm detectors produces an underestimate of the flux density: for objects as bright as 4 Jy, measured flux densities are likely to be ≃20% too low. This calibration has been checked against that of the *ISO* (using ULIRGs) and *IRAS* (using *IRAS*-derived diameters), and is consistent with those at the 5% level.

1. INTRODUCTION

MIPS (Rieke et al. 2004) is the far-infrared imager on the *Spitzer Space Telescope* (Werner et al. 2004). MIPS has three photometric channels, at 24, 70, and 160 μm. Like the other *Spitzer* instruments, the primary flux density calibrators at 24 and 70 μm are stars (IRAC: Reach et al. 2005; Fazio et al. 2004; Hora et al. 2004; and IRS: Houck et al. 2004). The calibration for the MIPS 24 and 70 μm channels is presented in companion papers by G. H. Rieke et al. (2007, in preparation), Engelbracht et al. (2007; 24 μm) and Gordon et al. (2007; 70 μm). Here we present the calibration of the 160 μm channel and describe some unexpected challenges that had to be overcome in performing the calibration. The emission from astronomical targets at this long wavelength is particularly useful in characterizing the abundance of cold dust, which frequently dominates the total emission from galaxies (e.g., Gordon et al. 2006; Dale et al. 2005). The MIPS 160 μm channel has also contributed new insight into the sources responsible for the previously unresolved cosmic infrared background (Dole et al. 2006).

Very few calibrations exist in the 100–200 μm wavelength regime. The *Infrared Astronomical Satellite* (*IRAS*; Neugebauer et al. 1984; Beichmann et al. 1985) 100 μm channel, the 60–200 μm channels of the *ISO* Imaging Photopolarimeter (ISOPHOT; Schulz et al. 2002) aboard the *Infrared Space Observatory* (*ISO*), and the Diffuse Infrared Background Explorer (DIRBE, at 60 to 240 μm; Hauser et al. 1998) aboard the *Cosmic Infrared Background Explorer* (*COBE*; e.g., Fixsen et al. 1997) relied on observations of solar system targets for their absolute calibrations. The Far Infrared Absolute Spectrophotometer (FIRAS) on *COBE* relied on observations of an external calibration target (Mather et al. 1999). In the case of *IRAS*, the calibration relied on observations of asteroids to extrapolate the calibration of the 60 μm channel to 100 μm. In the case of ISOPHOT, a few asteroids were studied in great detail, and their emission was used as the basis of the absolute calibration (Müller & Lagerros 1998, 2002). The primary reason these previous missions relied on observations of asteroids (and planets) to calibrate their longest wavelength channels was sensitivity: the instruments could not detect enough stellar photospheres at adequate signal-to-noise ratio (S/N) over a wide enough range of flux densities to support a calibration. In part, that was because the instruments had large beams that were

[1] Steward Observatory, University of Arizona, Tucson, AZ.
[2] *Spitzer* Science Center, Mail Stop 220-6, California Institute of Technology, Pasadena, CA.
[3] Max-Planck-Institute, Garching, Germany.
[4] Materials Science Division, Lawrence Berkeley National Laboratory, Berkeley, CA.
[5] Department of Materials Science and Engineering, University of California, Berkeley, CA.

not well sampled by their detectors, leading to high confusion limits to their sensitivity.

The original intention was to calibrate the MIPS 160 μm channel using observations and photospheric models of stars. Compared to the earlier missions, the MIPS detectors and electronics are significantly more sensitive. Also, the MIPS pixel scale, 16″, fully samples the 40″ beam provided by *Spitzer*, resulting in lower confusion limits. After launch, the stellar calibration strategy was found to be unworkable because a bright, short-wavelength ghost image impinged on the array at nearly the same location as the 160 μm image (see below). The strategy we adopted was similar to that employed by *IRAS*, namely, to use observations of asteroids in all three MIPS channels to transfer the calibration from the MIPS 24 and 70 μm channels to the 160 μm channel.

2. THE NEAR-IR GHOST IMAGE PROBLEM

Initial 160 μm commissioning observations of stars seemed to indicate that the array was 10–15 times more responsive than expected from prelaunch models and instrument characterization tests. However, observations of cold sources seemed to confirm the expected responsivity of the array. Within 4 months of the launch of *Spitzer*, we concluded that for targets with stellar near-IR : 160 μm colors, near-IR photons (with wavelengths $\simeq$1.6 μm) were forming a ghost image on the 160 μm array.

The Ge detectors are sensitive to near-IR light because of their intrinsic photoconductive response. The desired response to 160 μm light, on the other hand, arises from the extrinsic photoconductive response (achieved by doping with Ga) coupled with mechanical stress applied to the pixels (which extends the response from the normal 100 μm cutoff to about 200 μm). Optical modeling eventually indicated that near-IR photons diffusely reflected off the surface of the 160 μm short-wavelength blocking filter were responsible for the ghost image. That filter lies near an intermediate focus in the optical train, and the reflected photons form a poorly focused ghost image on the array. By design, the blocking filter is tilted relative to the light path to prevent specularly reflected near-IR light from impinging on the array. However, roughness on the surface of the blocking filter contributes a diffuse component to the reflected near-IR light, and it is this diffusely reflected light that forms the ghost image.

The near-IR light reflected from the blocking filter passes through the 160 μm bandpass filter (which has transmission in the near-IR of about 10^{-3}), but does not pass through the blocking filter. As a result, the ghost image is quite bright in spite of the diffuse nature of the reflection, having an intensity 10–15 times greater than the intensity of the 160 μm image for sources with stellar colors. The fact that the ghost image nearly coincides with the image of 160 μm light on the array (see Fig. 1) made it difficult to identify the problem in the first place, and also makes it very difficult to calibrate the relative strengths of the two images. Their relative strengths also depend on the temperature of the source. For a blackbody source spectrum (and assuming that the effective wavelength of the ghost image is 1.6 μm), objects with temperatures $\geq$2000 K will suffer from a ghost image comparable to or greater in brightness than the 160 μm image. Several attempts have been made to over-

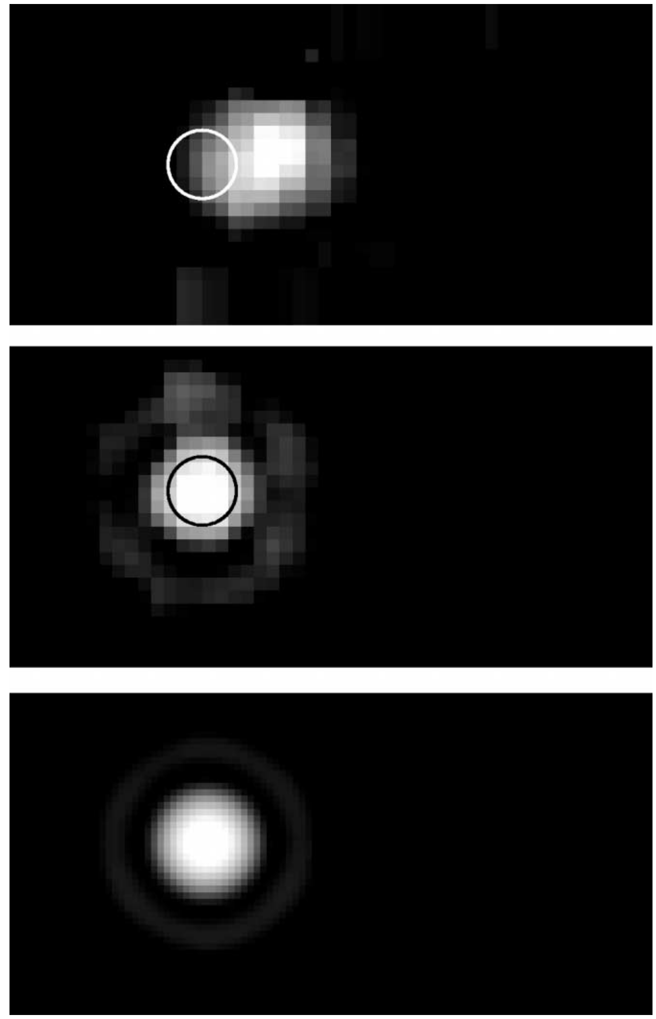

FIG. 1.—MIPS 160 μm images of a star (HD 163588; *top*), an asteroid (471 Papagena; *middle*), and an STinyTim–based model PSF (*bottom*). The star image is dominated by the near-IR ghost image (see text), while the asteroid image reveals no measurable contamination from the ghost image. For typical asteroids, the ghost image will be $\gtrsim$2000 times fainter, relative to the 160 μm image, than for stars. The circles are centered at the pointing used in each observation. The ghost image is always offset from the nominal pointing toward the array center line. The slightly different FOV of the two images (note missing data and replicated pixels around the edge of the mosaic of the star) results from the use of a small (three-point) map for the asteroid observation. The mosaics were generated using a pixel scale of 8″, $\simeq\frac{1}{2}$ the native pixel scale of the 160 μm array. The model PSF was generated using STinyTim (see text) with a pixel scale of 3.2″ and then smoothed using a boxcar 8 pixels (25.6″) in width, equivalent to 1.6 native pixels. Each image is 6.5′ across; the circles in the upper panels are 40″ across.

come these uncertainties and difficulties and to characterize and calibrate the ghost image directly, but have met with quite limited success.

3. REVISED CALIBRATION STRATEGY

Asteroids were chosen as the new calibrators because of their very red near-IR to 160 μm color, their ubiquity, and their range of brightness. For typical asteroids the brightness of the ghost image will be at least 2000 times fainter than the 160 μm image, and so will not measurably affect any calibration based on observations of asteroids. Unfortunately, asteroids also have several qualities that detract from their attraction as calibrators: their far-IR SEDs are difficult to predict (due to temperature variations across and within the surface), are time-variable (due to rotation and changing distance from the Sun and observer), and are poorly characterized at far-IR wavelengths. L and T dwarfs cannot be used because they are far too faint to be detected using MIPS at 160 μm.

Because of the difficulty in predicting the 160 μm flux density from a given asteroid for a particular observing circumstance, we adopted a calibration strategy that relies on near-simultaneous observations of asteroids at 24, 70, and 160 μm, and then bootstraps the 160 μm calibration from the well-understood calibrations at 24 and 70 μm. In addition, we have observed many asteroids so that we can use the average properties of the data to derive the calibration, rather than rely on detailed efforts to model the thermal emission of individual asteroids. The emission from asteroids at wavelengths beyond 60 μm has only been characterized for a few objects (e.g., Müller & Lagerros 1998, 2002), but those objects are all far too bright to observe with MIPS.

3.1. Faint and Bright Samples

Because the far-IR SEDs of asteroids are not well studied, we felt that it was very important to characterize the thermal emission of our calibration targets at both 24 and 70 μm to predict their emission at 160 μm. However, saturation limits introduce a complication in trying to observe any particular asteroid in all three MIPS channels. For a typical asteroid, the ratio of the flux densities, $24:70:160$ μm, is about $10:3:0.8$. The 24 μm channel saturates at 4.1 Jy in 1 s, and somewhat brighter sources can be observed using the first-difference image, which has an exposure time of 0.5 s. This limits the maximum 160 μm brightness that can be related back to well-calibrated 24 μm observations to about 0.5 Jy. Sensitivity and confusion limits at 160 μm require that we observe asteroids brighter than about 0.1 Jy at 160 μm. Thus, the dynamic range of the 160 μm fluxes that can be directly tied to 24 μm observations is only a factor of 5, from 100 to 500 mJy. The hard saturation limit at 70 μm, 23 Jy, does not place any restriction on sources that can be observed at both 70 and 160 μm (the 160 μm saturation limit, 3 Jy, is about $\frac{1}{2}$ of the 160 μm flux density from an asteroid with a 23 Jy 70 μm brightness). These saturation-related restrictions lead us to adopt a two-tiered observation and calibration strategy.

Faint asteroids: 24 μm *sample*.—We observe asteroids predicted to be fainter than ∼4 Jy at 24 μm in all three MIPS channels. The data are taken nearly simultaneously (typically less than 30 minutes to observe all three channels, with nearly all of that time being devoted to taking the 160 μm data). The short duration of the observations limits potential brightness variations due to rotation of the target (in addition, the targets were selected on the basis of not exhibiting strong visible light-curve variations). We then use the observed flux densities at 24 and 70 μm to predict the flux density at 160 μm using a thermal model (see below). We also compute the ratio of the *measured* 70 μm flux density to the 160 μm *model prediction*, and use that ratio later to predict the 160 μm flux density for asteroids too bright to observe at 24 μm.

Bright asteroids: 70 μm *sample*.—For asteroids predicted to be brighter than ∼4 Jy at 24 μm, we observe only at 70 and 160 μm. We then use the average $70:160$ color from the faint sample to predict the 160 μm flux density from the 70 μm observation. This sample extends the available dynamic range of the 160 μm observations by more than a factor of 2 relative to the 24 μm sample alone, allowing us both to measure the calibration factor up to the 160 μm saturation limit and to determine whether the response is linear.

3.2. Limitations

This strategy is subject to some limitations, in addition to uncertainties inherent to all absolute calibration schemes. The calibration we derive at 160 μm is wholly dependent on the MIPS calibrations at 24 and 70 μm, and its accuracy cannot exceed the accuracy of the calibration of those channels. As described in Engelbracht et al. (2007), the absolute calibration at 24 μm is good to 2%; Gordon et al. (2007) show that the 70 μm absolute calibration is good to 5.0%. These absolute calibration uncertainties in the shorter channels translate into a 7% uncertainty on the predicted 160 μm flux density of any object with a $24:70$ μm color temperature of around 250 K (as our targets do). This represents the ultimate theoretical accuracy of the 160 μm calibration we can derive via the methods described here.

As mentioned above, the dynamic range of the 160 μm fluxes that we can relate to objects observed at both 24 and 70 μm is quite small. Thus, the bright sample is critical for extending the dynamic range of the calibration. However, our predicted 160 μm fluxes rely on the average $70:160$ μm model color of the faint sample, so the calibration is dependent on the uncertainty in that color. The S/N of our measurements at the shorter wavelengths is typically in excess of 50, so their precision is not a major factor. However, the average $70:160$ μm color we use depends on what we assume for the spectral emissivity of asteroids. There are hints in the *ISO* data that the emissivity of some asteroids is depressed by ≃10% in the far-

IR (Müller & Lagerros 2002), and model-based predictions that surface roughness may also affect the slope of the far-IR thermal spectrum. Here we assume that asteroids emit as graybodies and use a thermal model that does not incorporate the effect of surface roughness on the slope, and the calibration we derive follows directly from that assumption. The full impact of all the uncertainties mentioned here on the accuracy of the calibration is discussed in § 8.1.

4. OBSERVATIONS AND DATA ANALYSIS

4.1. The Observations

For each MIPS observing campaign, we used the JPL Solar System Dynamics division's HORIZONS system to select main-belt asteroids within the *Spitzer* operational pointing zone.[6] From this set, we selected objects with an albedo and diameter in the HORIZONS database (primarily derived from the *IRAS* asteroid catalog; Tedesco et al. 2002). For the purposes of observation planning only, we used the *IRAS* albedos and diameters to predict flux densities in the MIPS channels. We typically selected a few to observe, picking those that could be observed in a reasonable amount of time, that would not saturate the detectors, and that did not have significant light-curve amplitudes (again, as indicated by the HORIZONS database).

The 28th MIPS observing campaign comprised 102 individual observations of asteroids (between 2003 December and 2006 January). Of those, 79 resulted in 160 μm detections with S/N $\geq$ 4; 33 of those were three-color (24, 70, and 160 μm) observations of fainter asteroids; and 46 were two-color (70 and 160 μm only) of brighter objects. All observations were made using the MIPS photometry astronomical observing template (AOT), which provides dithered images to improve point-spread function (PSF) sampling and photometric repeatability. The 160 μm array is quite small, having an (unfilled) instantaneous field of view (FOV) of 0.8 by 5.3′. The photometry AOT, because of the dithers, results in a larger but still restricted 2.1′ × 6′ filled FOV for the final mosaic. The diameter of the first Airy minimum of the 160 μm PSF is 90″. After collecting 160 μm data using the standard dither pattern for a few observing campaigns, we began taking those data by combining the AOT with a small map. This provided more sky around the target and improved the sampling of the PSF. Figure 1 shows a sample 160 μm image for a bright asteroid resulting from such an observation.

4.2. Data Analysis

The data were analyzed using the MIPS instrument team data analysis tools (DAT; Gordon et al. 2005). These tools have been used to develop the reduction algorithms and calibration of the MIPS data, beginning during ground test and continuing through on-orbit commissioning and routine operations. The *Spitzer* Science Center data processing pipeline is used to independently verify the algorithms and calibrations developed through the instrument team DAT. Both the SSC pipeline and the DAT use the same calibration files (e.g., darks, illumination corrections) and the same absolute calibration factors. Comparison of 160 μm photometry for data processed through the DAT and the SSC pipeline show that the two agree to better than 1%. Data at 24 and 70 μm were reduced, and photometry extracted, in exactly the same manner as all other calibration data for those channels (see Engelbracht et al. 2007; Gordon et al. 2007). Because the exposure times at 24 and 70 μm were so short, the motion of the asteroids during those observations was insignificant relative to the beam size in all cases. At 160 μm the beam is typically much larger than target motion, even though the integration times in that channel were sometimes quite long. In the few instances where object motion during the 160 μm observation was significant (160 μm astronomical observation request [AOR] execution times approaching 1 hr), we generated mosaics in the comoving frame.

The basic processing of the 160 μm data is described in Gordon et al. (2005). Briefly, each observation consists of multiple, dithered images. During acquisition of each image, termed a data collection event (DCE), the signal from the pixels is nondestructively sampled every 1/8 s. The pixels were reset every 40th sample. Cosmic rays are identified as discontinuities in the data ramps, and slopes are then fit to the cleaned ramps. Because the responsivity of the Ge : Ga array varies with time and flux history, internal relative calibration sources (stimulators) are flashed every 8th DCE during data collection. Each slope image is then ratioed to an (interpolated and background-subtracted) stimulator image, and the result is corrected for the measured illumination pattern of the stimulators to produce a responsivity-normalized image for each dither position in an observation. Those images are mosaicked using world coordinate system information to produce a final image of the sky and target. The mosaics used in this analysis were constructed using pixels 8″ square, $\simeq\frac{1}{2}$ the native pixel scale of the 160 μm array. This subsampling provides better PSF sampling and aids in identifying outlier pixels during mosaicking. Because the slope image from each DCE is ratioed to a stimulator image, brightness in the resulting mosaics is in dimensionless instrumental units, which we will refer to as MIPS160 units, or simply MIPS160. The goal of the calibration program is to derive the conversion (the "calibration factor," or CF) between MIPS160 and surface brightness in units of, e.g., MJy sr^{-1}.

5. PHOTOMETRY AND APERTURE CORRECTIONS

Figure 2 shows an azimuthally averaged radial profile of an observed 160 μm PSF and compares it to model profiles generated using the *Spitzer* PSF software (STinyTim, ver. 1.3; Krist 2002). The measured profile is derived from the observation of the bright (2.3 Jy) asteroid Papagena (see Fig. 1); other observations result in very similar PSFs. Model PSFs were

[6] See http://ssd.jpl.nasa.gov.

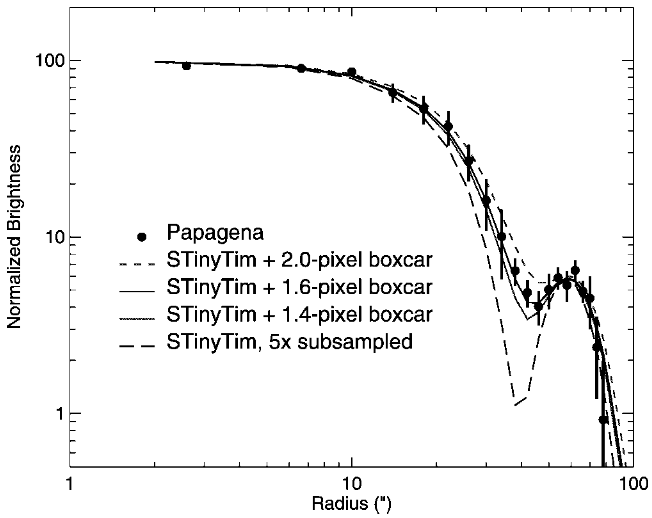

FIG. 2.—Observed 160 μm PSF radial profile compared to four STinyTim model PSF radial profiles. The observed profile (*circles*) is derived from the observation of asteroid 471 Papagena shown in Fig. 1; error bars indicate the scatter within each radial bin. The mosaic used to generate the profile has pixels 8″ square. The model PSFs were generated with 3.2″ square pixels (5 times oversampled). Various smoothings were then applied to the model PSF to match the shape of the observed PSF. Smoothing with a boxcar equivalent to 1.6 native pixels (25.6″) results in an excellent match with the observed PSF. The FWHM of the observed PSF is 38.3″, and for the model it is 38.2″.

TABLE 1

MIPS 160 μm APERTURE CORRECTIONS

TEMPERATURE (K)	APERTURE RADIUS (arcsec) 16	24	32	40	48	64
			No Sky Annulus			
10	4.761	2.657	2.011	1.776	1.634	1.402
30	4.677	2.610	1.976	1.745	1.605	1.355
50	4.665	2.603	1.971	1.740	1.601	1.348
150	4.651	2.595	1.965	1.735	1.596	1.341
250	4.648	2.593	1.963	1.734	1.595	1.340
500	4.648	2.593	1.963	1.734	1.595	1.339
2000[a]	4.645	2.592	1.962	1.733	1.594	1.339
			With Sky Annulus[b]			
10	4.785	2.670	2.021	1.785	1.642	1.406
30	4.697	2.621	1.984	1.752	1.612	1.361
50	4.683	2.613	1.978	1.747	1.607	1.354
150	4.668	2.605	1.972	1.741	1.602	1.348
250	4.665	2.603	1.971	1.740	1.601	1.347
500	4.662	2.602	1.970	1.739	1.600	1.346
2000[a]	4.662	2.602	1.970	1.739	1.600	1.345

[a] Note that sources with near-IR 160 μm color temperatures ≥2000 K are subject to additional, large photometric uncertainty due to the contribution from the near-IR ghost image.

[b] The sky annulus radius was 64″–128″ for apertures up to 48″, and 80″–160″ for the 64″ aperture.

generated assuming a source with a 250 K blackbody spectrum, consistent with the temperatures we find for our sample. The models were also generated using 5 times oversampling, resulting in model pixels 3.2″ square. As is seen for the other two MIPS channels (see Engelbracht et al. 2007; Gordon et al. 2007), the primary difference between the model and observed PSFs is in the region of the first Airy minimum. However, suitably smoothed, the model PSF represents the observed PSF quite well. This is reflected in Figure 1, where the overall morphology of the observed and model PSFs can be compared. Figure 2 compares the radial profiles for the observed and model PSFs and shows the good agreement between the two. The best-fit model PSF is smoothed using a boxcar with a width of 25.6″, corresponding to a width of 1.6 native pixels.

Because of the restricted FOV of the 160 μm images, we are forced to use small apertures for performing photometry (this is in contrast to the large apertures used to derive the 24 and 70 μm calibrations). Thus, the calibration at 160 μm depends more strongly on the aperture corrections. We computed aperture corrections based on the model PSF shown in Figures 1 and 2. The models offer two advantages over the observed PSF: they are noiseless, and there is no uncertainty associated with determining the background (particularly difficult at 160 μm because of the restricted FOV). The total flux in STinyTim model PSFs depends on the model FOV; we used models 128′ across in order to capture most of the flux in the far field of the PSF. We have extrapolated the PSF to 512′ using an Airy function and integrated over that much larger model to constrain the magnitude of any bias in our aperture corrections stemming from their finite FOV. Those calculations indicate that only 0.1% of the flux from a source falls in the region between 128′ and 512′; we conclude that our aperture corrections are not significantly biased by our use of the 128′ models. Later we show that our calibration, when applied to extended sources, gives results consistent with *ISO* to within 6%. That agreement provides some additional confidence in the accuracy of our aperture corrections.

Application of the model-based aperture corrections to observed PSFs revealed that for apertures ≤48″ in radius, the measured flux depended on aperture size. The reason is the small but systematic difference between the observed and model PSFs at radii of ≃10″–20″, which can be seen in Figure 2. To correct this, we have adopted a hybrid approach to computing the aperture corrections, using the smoothed model PSFs for apertures with radii ≥48″, and observed PSFs for smaller apertures. We used observations of nine asteroids observed using a small 160 μm map (giving a somewhat larger FOV, as noted earlier), and with fluxes near 1 Jy for the computation. (We also compared these asteroid-based corrections to those based on Pluto [with a color temperature of 55–60 K], and found no measurable difference.) The empirical corrections are normalized to the model correction for the 48″ aperture. Table 1 lists the resulting hybrid aperture corrections for a selection of photometric aperture sizes, with and without sky annuli, and for a range of source temperatures. Note that these corrections can only accurately be used for sources that are

TABLE 2
MIPS Color Corrections

Parameter	λ_0 (23.68 μm)	λ_0 (71.42 μm)	λ_0 (155.9 μm)
Blackbody Spectrum			
T (K):			
10,000.0	1.000	1.000	1.000
1000.0	0.992	0.995	0.999
300.0	0.970	0.980	0.996
150.0	0.948	0.959	0.991
100.0	0.947	0.938	0.986
80.0	0.964	0.923	0.982
70.0	0.986	0.914	0.979
60.0	1.029	0.903	0.976
50.0	1.119	0.893	0.971
40.0	1.335	0.886	0.964
35.0	1.569	0.888	0.959
30.0	2.031	0.901	0.954
25.0	3.144	0.941	0.948
20.0	7.005	1.052	0.944
Power Law (ν^β)			
β:			
−3.0	0.967	0.933	0.965
−2.0	0.960	0.918	0.959
−1.0	0.961	0.918	0.959
0.0	0.967	0.932	0.965
1.0	0.981	0.959	0.979
2.0	1.001	1.001	1.000
3.0	1.027	1.057	1.029

Note.—Divide measured fluxes by these values to compute the corrected monochromatic flux density.

relatively cold (significantly less than 2000 K)—otherwise, the near-IR ghost image both alters the PSF and becomes comparable to or brighter than the 160 μm image. We have verified that the corrections in Table 1 result in photometry that is independent of aperture size by analyzing 29 cluster-mode asteroid observations, where the targets ranged in brightness from 0.1 to 4 Jy. The variation with aperture size shows no monotonic trend, and the results for all apertures agree to within 1%.

We performed photometry on our 160 μm images using an aperture 24″ in radius. The small aperture allowed us to increase the S/N of our photometry for the faintest asteroids and thereby to extend the calibration to somewhat fainter flux densities than would have been possible otherwise. The aperture photometry was corrected to total counts using the aperture correction in Table 1. Photometry at 24 and 70 μm was performed exactly as it was to derive the calibrations in those channels, and as described in Engelbracht et al. (2007) and Gordon et al. (2007). Because a number of our brightest asteroids were in the nonlinear response regime at 70 μm (i.e., above a few janskys), we have used PSF fitting (using the StarFinder package; Diolaiti et al. 2000) to do all of the 70 μm photometry used here. We attempted to analyze the 160 μm data using PSF fitting as well, but the resulting photometry displayed more scatter than did the aperture photometry. We believe this was due to the restricted FOV of the mosaics, and the presence of spatial structure (artifacts) in the images, particularly for fainter sources. An area of concentration in the future will be implementing more robust PSF-fitting algorithms for use at 160 μm.

6. COLOR CORRECTIONS

The effective wavelengths of the MIPS channels, defined as the average wavelength weighted by the spectral response function, $R(\lambda)$, are $\lambda_0 = 23.68$, 71.42 and 155.9 μm. The color corrections, which correct the observed in-band flux to a monochromatic flux density at the effective wavelength, are defined by

$$K = \frac{[1/F(\lambda_0)]\int F(\lambda)R(\lambda)\,d\lambda}{[1/G(\lambda_0)]\int G(\lambda)R(\lambda)\,d\lambda}.$$

Here $F(\lambda)$ is the spectrum of the source, $G(\lambda)$ is the reference spectrum, λ is wavelength, F and G are in units of photons s^{-1} cm^{-2} μm^{-1}, and R is in units of e^- photon^{-1}. As defined here, the observed flux should be divided by K to compute the monochromatic flux density. The MIPS response functions can be obtained from the *Spitzer* Web site.[7] For MIPS, the reference spectrum G is chosen as a 10^4 K blackbody. While we refer to the 24, 70, and 160 μm channels, we have used the actual effective wavelengths of those channels for all quantitative analyses. For reference, the zero-magnitude flux density at 155.9 μm is 160 ± 2.45 mJy. Because the asteroids are much colder (with typical 24 : 70 μm color temperatures around 250 K), we had to apply color corrections to convert the measured fluxes to monochromatic flux densities at the effective wavelengths. The color corrections for all three MIPS channels and representative source spectra are given in Table 2. In all three channels they are slowly varying functions of temperature above temperatures of 100 K and also deviate only a few percent from unity at those temperatures. For objects with data at both 24 and 70 μm, the color corrections were computed iteratively, based on the 24 and 70 μm flux densities. For the brighter targets lacking 24 μm data, we assumed a temperature of 251 K (see Fig. 4) and applied the corresponding color correction.

7. THERMAL MODELING

The standard thermal model (STM; Lebofsky & Spencer 1989) is the most widely used (therefore "standard") model for interpreting observations of thermal emission from small bodies in the asteroid main belt and the outer solar system (see Campins et al. 1994; Tedesco et al. 2002; Fernandez et al. 2002; Stansberry et al. 2006). The model assumes a spherical body whose surface is in instantaneous equilibrium with the insolation, equivalent to assuming a thermal inertia of zero, a nonrotating body, or a rotating body illuminated and viewed

[7] See http://ssc.spitzer.caltech.edu/mips.

pole-on. In the STM the subsolar point temperature is

$$T_0 = \left[\frac{S_0\,(1 - p_V q)}{(\eta\epsilon\sigma)}\right]^{1/4}, \quad (1)$$

where S_0 is the solar constant at the distance of the body, p_V is the geometric albedo, q is the phase integral (assumed here to be 0.39, equivalent to a scattering asymmetry parameter, $G = 0.15$ [Lumme & Bowell 1981; Bowell et al. 1989]), η is the beaming parameter, ϵ is the emissivity (which we set to 0.9), and σ is the Stefan-Boltzmann constant. Given T_0, the temperature as a function of position on the surface is $T = T_0\mu^{1/4}$, where μ is the cosine of the insolation angle. The nightside temperature is taken to be zero. Surface roughness leads to localized variations in surface temperature and nonisotropic thermal emission (beaming). When viewed at small phase angles, rough surfaces appear warmer than smooth ones because the emission is dominated by warmer depressions and sunward-facing slopes. This effect is captured by the beaming parameter η. Lebofsky et al. (1986) found $\eta = 0.76$ for Ceres and Vesta; the nominal range for η is 0–1, with unity corresponding to a perfectly smooth surface (Lebofsky & Spencer 1989).

The purpose of our thermal modeling is to use the measured 24 and/or 70 μm flux densities to predict the 160 μm flux density for that target. First we correct the flux density from the observed phase angle (typically about 20° for our targets) to 0° using a thermal phase coefficient of 0.01 mag deg^{-1} (e.g., Lebofsky & Spencer 1989). We then use the absolute visual magnitude (H_V, defined for a phase angle of 0°) from HORIZONS and the relation (e.g., Harris 1998) $D = 1329 \times 10^{-H_V/5}\, p_V^{-1/2}$ to compute the target diameter (where D is the diameter in kilometers, and p_V is the visible geometric albedo). Target diameter and albedo are varied until a fit to the observed flux density is achieved. For targets observed at both 24 and 70 μm, the beaming parameter is also varied in order to simultaneously fit both MIPS bands and the visual magnitude. The fitted physical parameters are then fed back into the STM to predict the 160 μm flux density.

Figure 3 illustrates the measured SED for one of our targets. Also shown are a blackbody and STM fit to the 24 and 70 μm points. The blackbody and STM fits are indistinguishable at the MIPS wavelengths, but small deviations can be seen on the short-wavelength side of the emission peak. For the purpose of calibrating the 160 μm channel, we simply require a reliable way to predict the 160 μm flux density by extrapolation from the shorter wavelengths. As the figure demonstrates, the details of the short-wavelength SED do not appreciably affect the predicted 160 μm flux density. Indeed, we have performed the calibration using both STM and blackbody predictions, and the results are consistent with each other to within better than 1%.

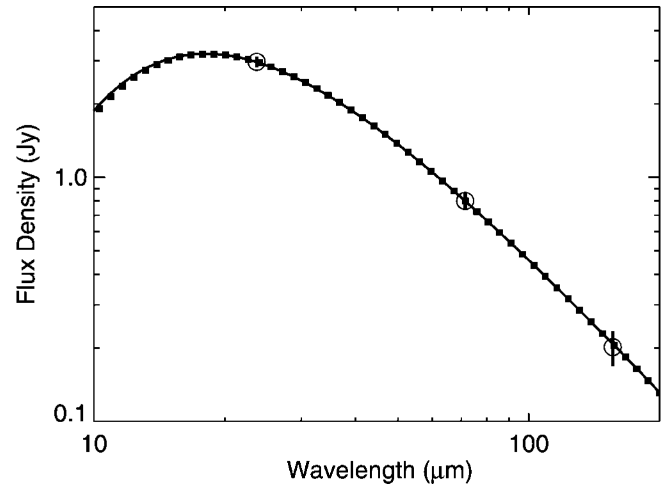

FIG. 3.—SED for asteroid 282 Clorinde compared to blackbody and STM fits. The measured SED in the MIPS channels is shown as circles with error bars (the error bars are the rss of the measurement uncertainty determined from the images and the calibration uncertainties in each channel). The squares trace a blackbody fit to the data; the solid line shows the STM fit. The 160 μm point is plotted using the calibration derived here, but was not used in the fits.

8. RESULTS

8.1. The 24 μm Subsample

Table 3 summarizes our measurements of targets in the 24 μm sample. Aperture- and color-corrected flux densities are given for the 24 and 70 μm measurements. The 160 μm data are given in the instrumental units, MIPS160, described in § 4.2. As for the shorter wavelengths, the 160 μm measurements have been aperture- and color-corrected. The 24 μm sample makes up one-half of the full data set, and covers the faint end of the sample. These observations also allow us to directly determine the color temperatures (used to compute color corrections for individual observations within the sample) and to predict an average color temperature (used to compute color corrections for the 70 μm sample). We also use the 24 μm sample to compute the average 70 : 160 μm model color for asteroids, which we use to predict 160 μm fluxes for the 70 μm sample.

Figure 4 shows the color temperatures of the objects in the 24 μm sample, determined by fitting a blackbody to the photometry in those channels. The temperatures are fairly tightly clustered, with an average and standard deviation of $\simeq$251 ± 25.6 K. The temperatures are plotted versus predicted 160 μm flux density. In the context of this figure (only), the prediction is simply the extrapolation of the fitted blackbody curve to 160 μm. Although the range of predicted 160 μm flux densities for the 24 μm sample is only a factor of 5, there is no apparent trend of color temperature. Because the temperatures are fairly similar among all the targets, the predicted 160 μm flux density is to first order a measure of the overall apparent thermal brightness of the targets. It then reflects a combination of the influences of distance (helio- and *Spitzer*-centric), albedo, and size. It might be expected that if any of these things were biasing our results or imposing a systematic trend in the predicted 160 μm flux density (e.g., if our brightest targets were systematically hotter), it would be apparent in this figure.

TABLE 3
24 μm (Faint) Sample

No.	Asteroid	Obs. Date	AORKEYS[a] 24+70	AORKEYS[a] 160	F_{24}[b]	Err_{24}[b]	F_{70}[b]	Err_{70}[b]	P_{160}[b]	Err_{P160}[b]	MIPS160[c]	Err_{M160}[c]	CF[d]
186	Celuta	2004 Feb 23	...	9064960	4.612	0.231	1.345	0.139	0.356	0.049	1.516	0.406	38.99
248	Lameia	2004 Feb 23	...	9065216	3.585	0.179	1.082	0.115	0.288	0.041	1.516	0.491	31.60
443	Photographica	2004 Feb 23	...	9065728	2.089	0.104	0.584	0.063	0.153	0.022	0.628	0.390	40.46
186	Celuta	2004 Mar 18	...	9193216	2.700	0.135	0.902	0.093	0.246	0.034	1.053	0.377	38.82
25	Phocaea	2004 Mar 18	...	9193728	3.618	0.181	1.138	0.117	0.306	0.042	1.961	0.869	25.93
432	Pythia	2004 Mar 18	...	9193984	3.186	0.159	1.127	0.116	0.311	0.042	0.827	0.372	62.50
284	Amalia	2004 Apr 7	...	9460224	3.805	0.190	1.086	0.112	0.286	0.039	1.196	0.249	39.72
783	Nora	2004 Apr 7	...	9460736	6.159	0.308	1.895	0.195	0.507	0.069	1.827	0.445	46.09
432	Pythia	2004 Apr 7	...	9460992	2.329	0.116	0.589	0.062	0.151	0.021	0.848	0.224	29.55
1584	Fuji	2004 Apr 8	...	9460480	1.574	0.079	0.433	0.046	0.113	0.016	0.718	0.223	26.16
1584	Fuji	2004 May 2	...	9664512	0.993	0.050	0.242	0.027	0.061	0.009	0.577	0.159	17.71
60	Echo	2004 May 7	...	9665792	2.890	0.145	0.869	0.091	0.231	0.032	0.992	0.234	38.78
1137	Raissa	2004 May 7	...	9666048	0.654	0.033	0.189	0.022	0.050	0.008	0.328	0.114	25.22
1584	Fuji	2004 Jun 2	...	9810176	0.557	0.028	0.199	0.022	0.055	0.008	0.309	0.110	29.62
453	Tea	2004 Jun 2	...	9809920	1.572	0.079	0.532	0.055	0.145	0.020	0.709	0.178	34.12
113	Amalthea	2004 Jun 4	...	9810432	2.371	0.119	0.878	0.091	0.244	0.034	0.997	0.227	40.77
623	Chimaera	2004 Jun 18	...	9935104	2.318	0.116	0.751	0.077	0.203	0.028	0.773	0.176	43.69
572	Rebekka	2004 Jun 19	...	9935360	0.820	0.041	0.296	0.033	0.082	0.012	0.337	0.115	40.55
273	Atropos	2004 Jun 22	...	9934848	1.672	0.084	0.468	0.049	0.123	0.017	0.698	0.162	29.20
623	Chimaera	2004 Jul 9	...	10085120	1.353	0.068	0.448	0.047	0.122	0.017	0.569	0.150	35.58
138	Tolosa	2004 Jul 9	...	10084864	5.888	0.294	2.144	0.218	0.595	0.080	2.197	0.449	45.01
234	Barbara	2004 Jul 29	...	11779328	2.735	0.137	0.818	0.085	0.217	0.030	0.825	0.183	43.82
376	Geometria	2004 Aug 23	...	11896576	2.291	0.115	0.803	0.082	0.221	0.030	0.814	0.193	45.12
376	Geometria	2004 Aug 24	...	11896832	2.278	0.114	0.706	0.072	0.189	0.026	0.483	0.181	65.06
364	Isara	2004 Sep 21	...	12058624	3.301	0.165	0.789	0.084	0.200	0.028	0.541	0.236	61.34
189	Phthia	2004 Sep 21	...	12058112	2.699	0.135	0.766	0.079	0.201	0.028	0.512	0.213	65.34
856	Backlunda	2004 Oct 14	...	12428544	2.642	0.132	0.769	0.080	0.203	0.028	0.867	0.254	38.95
364	Isara	2004 Oct 14	...	12232448	4.706	0.235	1.171	0.121	0.299	0.041	0.766	0.322	64.89
1137	Raissa	2004 Oct 14	...	12232960	1.215	0.061	0.388	0.041	0.105	0.015	0.524	0.138	33.18
60	Echo	2004 Nov 4	...	12393728	3.204	0.160	0.953	0.100	0.253	0.035	1.060	0.223	39.70
60	Echo-1	2004 Nov 4	...	12544000	3.285	0.164	1.064	0.109	0.288	0.039	1.116	0.241	42.88
60	Echo-2	2004 Nov 4	...	12544512	3.209	0.160	0.965	0.100	0.257	0.035	1.113	0.241	38.35
189	Phthia	2004 Nov 5	...	12393984	2.035	0.102	0.583	0.061	0.154	0.021	0.759	0.187	33.60
131	Vala	2004 Nov 29	...	12870656	1.364	0.068	0.361	0.040	0.093	0.014	0.409	0.114	37.94
198	Ampella	2004 Dec 2	...	12870144	2.823	0.141	0.881	0.091	0.236	0.032	0.860	0.186	45.67
198	Ampella	2005 Jan 2	...	13070336	4.228	0.211	1.379	0.141	0.374	0.051	1.270	0.270	48.89
470	Kilia	2005 Jan 2	...	13070848	1.764	0.088	0.581	0.060	0.158	0.022	0.593	0.203	44.20
248	Lameia	2005 Jan 2	...	13070592	3.040	0.152	0.907	0.094	0.241	0.033	1.311	0.305	30.56
376	Geometria	2005 Jan 24	13107456	13107200	1.391	0.070	0.452	0.048	0.122	0.017	0.593	0.137	34.29
556	Phyllis	2005 Jan 24	13107968	13107712	2.208	0.110	0.557	0.059	0.142	0.020	0.416	0.116	56.99
757	Portlandia	2005 Jan 29	13108480	13108224	2.932	0.147	0.958	0.099	0.260	0.035	0.887	0.193	48.65
443	Photographica	2005 Mar 1	13307648	13307392	1.525	0.076	0.467	0.050	0.125	0.018	0.241	0.212	86.22
495	Eulalia	2005 Mar 2	13308160	13307904	2.697	0.135	0.746	0.077	0.195	0.027	0.887	0.232	36.53
512	Taurinensis	2005 Mar 2	13307136	13306880	0.977	0.049	0.238	0.026	0.061	0.009	0.204	0.445	49.38
443	Photographica	2005 Apr 5	13443840	13443584	2.615	0.131	0.682	0.071	0.176	0.024	0.872	0.315	33.55
118	Peitho	2005 May 14	13637120	13636864	4.531	0.227	1.217	0.126	0.316	0.043	1.206	0.262	43.54
584	Semiramis	2005 May 14	13636608	13636352	2.578	0.129	0.805	0.084	0.216	0.030	1.141	0.257	31.47
435	Ella	2005 May 15	13637632	13637376	4.176	0.209	1.257	0.129	0.335	0.046	1.345	0.288	41.38
282	Clorinde	2005 Jun 18	15244800	15244544	3.021	0.151	0.824	0.087	0.215	0.030	0.840	0.193	42.50
126	Velleda	2005 Jun 18	15245824	15245568	3.969	0.198	0.976	0.101	0.248	0.034	1.194	0.257	34.59
877	Walkure	2005 Jun 18	15245312	15245056	4.043	0.202	1.139	0.117	0.299	0.041	1.252	0.262	39.68

[a] Unique identifier for data in the *Spitzer* archive. Where only the 160 AORKEY is given, the same key applies to the 24 and 70 μm data.

[b] Color-corrected flux densities and uncertainties, in janskys. The uncertainties include the uncertainty in the absolute calibration of the 24 and 70 μm bands (2% and 5%, respectively).

[c] Color-corrected 160 μm channel flux density and uncertainty, in instrumental units.

[d] Calibration factor derived from each observation, in MJy sr^{-1} $MIPS160^{-1}$.

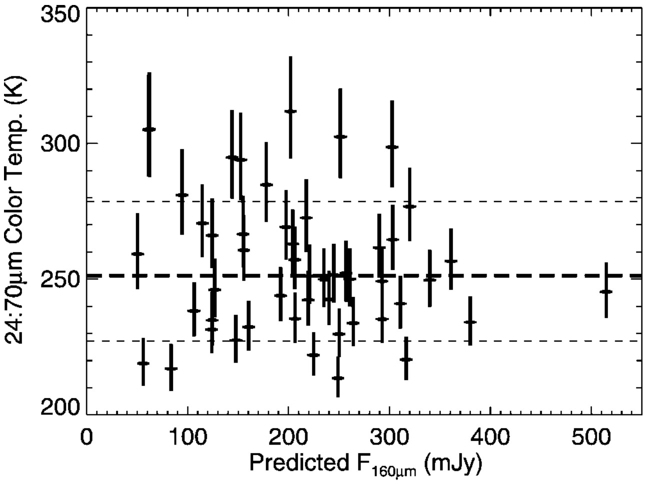

FIG. 4.—Color temperature of those asteroids faint enough to be observed at 24 μm. The color temperature is computed by fitting the 24 and 70 μm photometry with a blackbody. Error bars are computed by fitting a blackbody to the flux densities $\pm 1\ \sigma$. The average 24 : 70 color temperature is 251 K, and the rms deviation is 26 K (*thin dashed lines*).

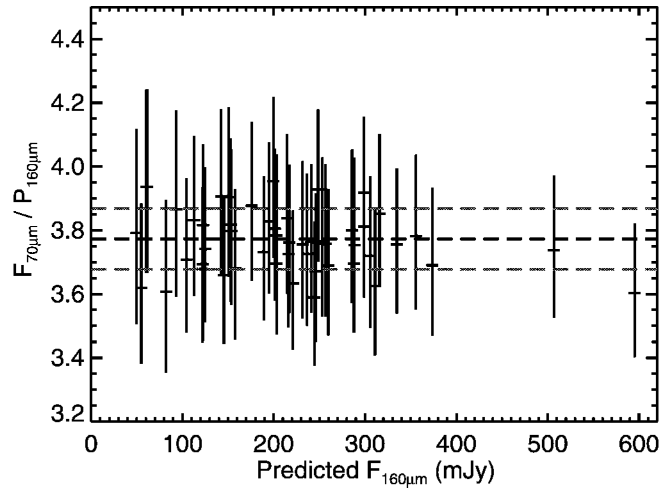

FIG. 5.—Ratio of the measured 70 μm flux density to the 160 μm flux density predicted from STM fits to the 24 and 70 μm photometry for objects in the 24 μm (faint) sample. The average 70 : 160 μm model color (*dashed lines*) is 3.77 ± 0.095, where the uncertainty is computed as the rms scatter of the individual predictions. The formal error on the average color is 0.014, or about 0.4%.

Given the fairly narrow range of color temperatures we see for the objects in the 24 μm sample, and the insensitivity of the model spectra from 24 to 160 μm to details of the thermal models, we expect the 70 : 160 μm color of the asteroids to be quite constant. Figure 5 shows the ratio of the measured 70 μm flux density to the predicted 160 μm flux density for each asteroid in the 24 μm sample. As expected, the color is tightly clustered, with a mean value of 3.77 and a rms scatter of 0.095, or 2.5%. Under the assumption that asteroids do not possess any strong emissivity variations versus wavelength in the far-IR, we use this color ratio to interpret our data for the brighter asteroids.

8.2. The 70 μm Subsample

Table 4 summarizes our measurements of targets in the 70 μm sample and is exactly like Table 3 except for the lack of 24 μm data. Making use of the average 70 : 160 μm color from the 24 μm sample, we compute the predicted 160 μm flux density for the 70 μm sample. The uncertainty on the 160 μm prediction is derived from the uncertainty in the 70 μm measurement root sum square (rss) combined with the 2.5% uncertainty in the average 70 : 160 color.

9. CALIBRATION FACTOR

Figure 6 shows the CF we derive from our observations of both the 24 and 70 μm samples, as a function of the predicted 160 μm flux density. The calibration factor is defined as the predicted flux density at 160 μm divided by the (aperture- and color-corrected) brightness in instrumental units (MIPS160), and by the area of a pixel in steradians.

Of the 102 individual observations, 23 were rejected on the grounds of having 160 μm $S/N < 4$; three more were rejected for having a measured 160 μm flux density more than twice the prediction (these were all for very bright sources), and the discrepancy is due to a poorly compensated nonlinear response in the 70 μm channel, resulting in predictions that were too low. Figure 6 shows the remaining 76 values of the calibration factor. There is a fairly clear trend of increasing calibration factor for predicted flux densities greater than about 2 Jy. We attribute this trend to a nonlinear response of the detectors for bright targets. This effect is similar in magnitude to that seen at 70 μm, also at flux densities greater than about 1–2 Jy (Gordon et al. 2007). For the moment we exclude the 19 points above 2 Jy from consideration. Taking the points below 2 Jy, we compute the average and rms scatter and identify as outliers eight points that deviate from the mean by more than 1.5 times that scatter (indicated by circled points in Fig. 6). We use the weighted mean of the remaining 49 values to compute the calibration factor for the MIPS 160 μm channel. Use of the weighted mean ensures that a source with zero flux produces zero response if all of the inputs to the calibration (e.g., dark current, linearity) are perfectly known.

The weighted mean calibration factor is CF $= 41.7$ MJy sr^{-1} MIPS160^{-1}, and the rms scatter is 4.82 MJy sr^{-1} MIPS160^{-1}. This suggests an uncertainty of 11.6% for the determination of the flux density of a particular source based on a single measurement. The formal uncertainty on the average calibration factor is 0.69 MJy sr^{-1} MIPS160^{-1}, or only 1.6%, but this value clearly underestimates the uncertainty that should be assumed when interpreting 160 μm photometry (see below). The average calibration factor and rms scatter are shown in Figure 6 as the horizontal dashed lines. Below we discuss other

TABLE 4
70 μm (BRIGHT) SAMPLE

No.	Asteroid	Obs. Date	AORKEYS[a] 70	AORKEYS[a] 160	F_{70}[b]	Err_{70}[b]	P_{160}[b]	Err_{P160}[b]	MIPS160[c]	Err_{M160}[c]	CF[d]
337 …….	Devosa	2003 Dec 13	…	8780288	5.573	0.285	1.476	0.057	4.056	0.307	60.49
1584 ……	Fuji	2003 Dec 13	…	8779520	0.478	0.025	0.127	0.057	0.603	0.063	34.90
752 …….	Sulamitis	2003 Dec 13	…	8780032	0.654	0.040	0.173	0.066	0.624	0.074	46.14
198 …….	Ampella	2004 Jan 25	…	8811776	2.667	0.144	0.706	0.060	2.585	0.108	45.43
83 ………	Beatrix	2004 Jan 25	…	8812032	3.384	0.182	0.896	0.059	3.830	0.142	38.90
345 …….	Tercidina	2004 Jan 25	…	8812288	4.336	0.233	1.149	0.059	4.913	0.232	38.85
25 ………	Phocaea	2004 Feb 23	…	9065472	1.425	0.087	0.378	0.066	1.342	0.199	46.77
345 …….	Tercidina	2004 Feb 23	…	9065984	6.478	0.338	1.716	0.058	6.106	0.216	46.71
783 …….	Nora	2004 Mar 18	…	9194240	0.996	0.056	0.264	0.062	1.641	0.441	26.72
60 ………	Echo	2004 Jun 1	…	9809408	1.458	0.078	0.386	0.059	1.192	0.132	53.85
18 ………	Melpomene	2004 Jun 18	…	9934592	5.618	0.290	1.488	0.057	5.069	0.173	48.79
7 ……….	Iris	2004 Jun 20	…	9934080	14.209	0.732	3.764	0.057	13.010	0.244	48.08
505 …….	Cava	2004 Jul 11	…	10084608	4.834	0.258	1.280	0.059	4.842	0.167	43.95
40 ………	Harmonia	2004 Jul 11	…	10084352	7.618	0.396	2.018	0.058	7.084	0.143	47.35
40 ………	Harmonia	2004 Jul 29	…	11779840	10.392	0.536	2.753	0.057	9.792	0.225	46.72
20 ………	Massalia	2004 Jul 29	…	11778816	6.575	0.338	1.742	0.057	6.406	0.153	45.18
40 ………	Harmonia	2004 Aug 23	…	11896064	13.304	0.683	3.524	0.057	12.246	0.202	47.83
20 ………	Massalia	2004 Aug 23	…	11895552	5.503	0.284	1.458	0.057	5.885	0.171	41.16
19 ………	Fortuna	2004 Sep 15	…	12057600	12.648	0.646	3.351	0.057	20.179	0.677	27.60
12 ………	Victoria	2004 Sep 22	…	12057088	3.295	0.176	0.873	0.059	7.575	2.197	19.15
3 ……….	Juno	2004 Sep 26	…	12059648	21.511	1.107	5.698	0.057	33.718	2.360	28.09
12 ………	Victoria	2004 Oct 14	…	12231936	4.941	0.256	1.309	0.058	5.977	0.437	36.39
313 …….	Chaldaea	2004 Nov 4	…	12393216	1.582	0.086	0.419	0.060	2.167	0.156	32.14
12 ………	Victoria	2004 Nov 4	…	12392704	5.369	0.275	1.422	0.057	9.404	0.938	25.14
433 …….	Eros	2004 Nov 29	…	12869120	2.212	0.115	0.586	0.058	2.069	0.104	47.09
83 ………	Beatrix	2005 Jan 2	…	13071360	6.339	0.328	1.679	0.058	5.682	0.152	49.12
433 …….	Eros	2005 Jan 2	…	13071104	3.578	0.185	0.948	0.058	3.070	0.116	51.31
21 ………	Lutetia	2005 Jan 24	13106944	13106688	7.806	0.401	2.068	0.057	7.566	0.184	45.42
12 ………	Victoria	2005 Mar 2	13306624	13306368	3.497	0.193	0.926	0.061	4.342	0.334	35.46
7 ……….	Iris	2005 Apr 12	13442304	13442048	13.522	0.700	3.582	0.058	18.829	1.420	31.62
42 ………	Isis	2005 May 16	13636096	13635840	11.057	0.567	2.929	0.057	8.648	0.174	56.29
6 ……….	Hebe	2005 Jun 18	15244288	15244032	13.356	0.685	3.538	0.057	11.163	0.208	52.67
471 …….	Papagena[e]	2005 Jul 27	15418112	15417856	10.433	0.535	2.764	0.057	10.070	0.188	45.61
471 …….	Papagena[e]	2005 Jul 27	15418624	15418368	12.347	0.634	3.271	0.057	10.317	0.163	52.69
471 …….	Papagena[e]	2005 Jul 27	15419136	15418880	11.598	0.595	3.072	0.057	10.002	0.171	51.05
23 ………	Thalia[e]	2005 Jul 28	15419648	15419392	2.914	0.152	0.772	0.058	2.987	0.143	42.94
23 ………	Thalia[e]	2005 Jul 28	15420160	15419904	3.283	0.172	0.870	0.058	2.897	0.138	49.88
23 ………	Thalia[e]	2005 Jul 28	15420672	15420416	3.122	0.163	0.827	0.058	3.327	0.099	41.30
313 …….	Chaldaea	2005 Aug 26	15813632	15813376	4.613	0.238	1.222	0.057	5.761	0.290	35.26
41 ………	Daphne	2005 Aug 27	15813120	15812864	7.544	0.388	1.999	0.057	7.634	0.184	43.51
138 …….	Tolosa	2005 Aug 29	15814656	15814400	2.023	0.108	0.536	0.059	2.035	0.106	43.78
433 …….	Eros	2005 Sep 4	15814144	15813888	0.509	0.032	0.135	0.068	0.968	0.308	23.18
42 ………	Isis[e]	2005 Nov 9	16259584	16258816	10.474	0.537	2.775	0.057	9.879	0.168	46.68
42 ………	Isis[e]	2005 Nov 9	16259840	16259072	12.191	0.624	3.229	0.057	9.869	0.199	54.38
42 ………	Isis[e]	2005 Nov 9	16260096	16259328	9.367	0.480	2.481	0.057	8.428	0.218	48.93
20 ………	Massalia[e]	2005 Nov 30	16465408	16464384	9.298	0.478	2.463	0.057	8.222	0.144	49.78
20 ………	Massalia[e]	2005 Nov 30	16465664	16464640	8.073	0.415	2.138	0.057	6.768	0.148	52.51
20 ………	Massalia[e]	2005 Nov 30	16465920	16464896	9.324	0.478	2.470	0.057	8.452	0.188	48.57
20 ………	Massalia[e]	2005 Nov 30	16466176	16465152	7.104	0.366	1.882	0.057	7.140	0.166	43.81
85 ………	Io	2006 Jan 11	16617984	16617728	5.520	0.286	1.462	0.058	5.973	0.148	40.69
51 ………	Nemausa	2006 Jan 12	16618496	16618240	9.987	0.511	2.645	0.057	9.389	0.210	46.83

[a] Unique identifier for data in the *Spitzer* archive. Where only the 160 AORKEY is given, the same key applies to the 70 μm data.

[b] Color-corrected flux densities and uncertainties, in janskys. The uncertainties include the uncertainty in the absolute calibration of the 24 and 70 μm bands (2% and 5%, respectively).

[c] Color-corrected 160 μm channel flux density and uncertainty, in instrumental units.

[d] Calibration factor derived from each observation, in MJy sr^{-1} $MIPS160^{-1}$.

[e] These objects were observed several times on the given date. The Papagena and Thalia observations were taken without interruption; those for Isis and Massalia were spaced by about 2 hr. Light-curve variations caused by the shape of these targets are predicted to contribute about 5% to the observed variation for all except Papagena, where the light curve should have only contributed about a 1% variation over the observing interval.

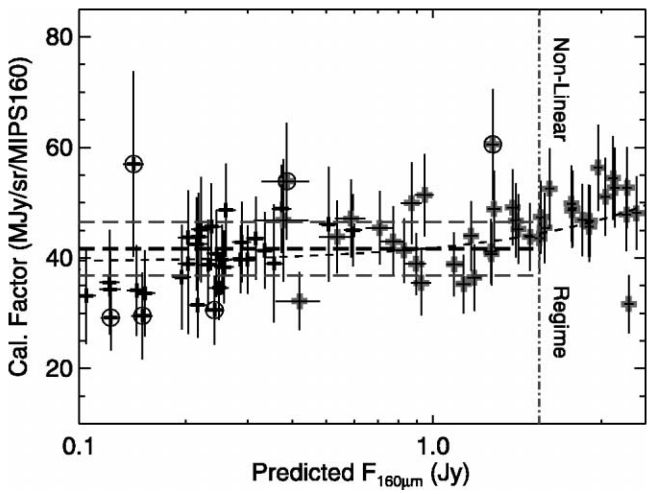

FIG. 6.—Calibration factor for the MIPS 160 μm channel vs. the predicted 160 μm flux density of the asteroids we observed. Black plus signs represent the objects in the 24 μm (faint) sample, which were observed at 24, 70, and 160 μm. Gray plus signs represent objects in the 70 μm (bright) sample, which was observed at 70 and 160 μm; 1 σ uncertainties are indicated by thin error bars. Data points that are circled were excluded from our calculation of the calibration factor because they are discrepant at or above 1.5 σ. Above about 2 Jy the response of the detectors becomes nonlinear, so the points above that are also excluded: formally, the calibration only applies below 2 Jy. The thick dashed line shows the weighted-average calibration factor, CF = 41.7 ± 0.69 MJy sr^{-1} $MIPS160^{-1}$. The rms scatter of the data is 4.82 MJy sr^{-1} $MIPS160^{-1}$, as shown by the thin, gray, long-dashed lines. The short-dashed line shows a linear fit to the data (including points >2 Jy), which yields CF = 39.2 ± 1.80 MJy sr^{-1} $MIPS160^{-1}$, with a slope of 2.58 ± 0.76 MJy sr^{-1} $MIPS160^{-1}$ Jy^{-1}. This calibration curve can be used to approximately calibrate targets with measured flux densities >2 Jy.

sources of uncertainty in the calibration. The final value and uncertainty we adopt are 41.7 ± 5.0 MJy sr^{-1} $MIPS160^{-1}$ (equivalent to a 12% uncertainty). This calibration is valid for sources with 155.9 μm flux densities ≤2 Jy.

We also computed a weighted linear fit to the data, but in this case include those points with predicted 160 μm flux densities >2 Jy. Based on the linear fit, CF = 39.24 + 2.58(P_{160}) MJy sr^{-1} $MIPS160^{-1}$, where P_{160} is the predicted 160 μm flux density. The formal uncertainties on the intercept and slope from the linear fit are 1.29 and 0.76 MJy sr^{-1} $MIPS160^{-1}$ Jy^{-1}, respectively, indicating that the slope is significant at the 3.4 σ level. This reflects the influence of the response nonlinearity above 2 Jy and can be used to provide an approximate calibration of targets with flux densities >2 Jy. Inspection of the points in Figure 6 suggests that the nonlinearity may affect photometry at the 20% level for targets with flux densities near 4 Jy, somewhat more than would be derived based on the linear fit to the data.

9.1. Uncertainty on the 160 μm Absolute Calibration

As suggested above, observers are typically more interested in the uncertainty they should assume for the flux density they determine from a single observation of a target than they are in the formal uncertainty on the calibration factor determined from an ensemble. Here we compare the 11.6% uncertainty estimated above to the uncertainty we would expect given the other uncertainties in the inputs to the calibration. The relevant uncertainties to consider are (1) the photometric repeatability at 160 μm, (2) the uncertainties in the 24 and 70 μm calibrations, (3) systematic uncertainties associated with color and aperture corrections, and (4) uncertainties inherent to the models used in the calibration.

We have assessed the photometric repeatability of the 160 μm channel two ways. Because we have relatively few repeated observations of stable (i.e., nonasteroidal), red sources, we analyzed 81 160 μm observations of a stellar calibrator (HD 163588) and found that those measurements exhibited an rms scatter of 3.4%. While those data are severely impacted by the short-wavelength ghost, they do provide a valid measure of the repeatability delivered by the readout electronics and the end-to-end data analysis for a very bright source. We have also analyzed five 160 μm observations of IRAS 03538−6432, which has a very red near-IR : 160 μm color and a 160 μm flux density of ≃1.04 Jy (Klaas et al. 2001), finding an rms scatter of 5.5%. We adopt 5% as our current estimate of the repeatability.

The uncertainties in the calibrations of the shorter MIPS bands are estimated to be 2% (24 μm: Engelbracht et al. 2007) and 5% (70 μm: Gordon et al. 2007). As noted earlier, taken in combination and ignoring any other uncertainties, these place a lower limit on the 160 μm calibration uncertainty of 7%. The color corrections we have applied are very modest (a few percent) and thus are unlikely to contribute significantly to the calibration uncertainty. The 24 and 70 μm photometry was done identically to the way it was done for the calibrations of those bands and thus should not impose any additional uncertainty or systematic bias on the results used here.

The 160 μm aperture correction we used, 2.60, is large and probably uncertain at the level of a few percent. Uncertainty in the aperture correction will be irrelevant if others use the same aperture (i.e., 24″, with a sky annulus of 64″–128″) and correction to perform photometry of point sources, and we encourage observers to use this aperture when practical. However, we cannot assume that such will be the case. Checks of 160 μm measurements of extended sources (see below) against previous missions show agreement to within about 6%, suggesting that our aperture corrections are reasonably accurate. As noted earlier, we find no evidence that the aperture correction for the 24″ aperture is any more uncertain than that for the 48″ aperture, where the aperture correction is a more modest (and model-based) 1.60. For lack of good 160 μm observations to further assess the uncertainty in the aperture corrections, and based on our experience with the 24 and 70 μm calibrations, we adopt an uncertainty of 3% for our 160 μm aperture corrections. This uncertainty should be interpreted as applying to the 48″ aperture, and as being empirically verified as transferable to the 24″ aperture.

The final uncertainty in the calibration is associated with the assumptions inherent in the STM, particularly the spectral emissivity in the 24–160 μm range. As noted earlier, we have assumed a gray emissivity, whereas there are suggestions from *ISO* observations that the emissivity of some asteroids may decline by 10% or so in this region (e.g., Müller & Lagerros 2002). We find that our 24 and 70 μm measurements of asteroids, when fit with the STM, give diameters for the targets that agree to within 3%. This suggests that there is no strong decrease of emissivity for the asteroids in our sample between 24 and 70 μm (because those calibrations are derived solely from observations of stars). Unfortunately, we cannot make a similar argument about emissivity in the range 70–160 μm based on our data. We adopt an uncertainty of 5% to account for our lack of knowledge of the spectral emissivity at 160 μm, and as being consistent with the lack of evidence for any measurable emissivity trend from 24 to 70 μm.

If we rss-combine the uncertainties just discussed, we predict that the 160 μm calibration should be accurate to 10.4%, which is very consistent with the 11.6% uncertainty estimated from the rms scatter of the calibration factor values in Figure 6. While the combined effect of the calibration uncertainties at 24 and 70 μm is the largest single contributor to the 160 μm uncertainty, the other uncertainties together are at least as important. Given that emissivity effects would result in a systematic bias in our calibration, we should not really rss it with the other uncertainties. If we rss-combine the other uncertainties and then simply add the 5% uncertainty for emissivity effects, we predict a worst-case uncertainty of 14.1% in the calibration ("worst-case" because it assumes that the net effect of the random uncertainties combine constructively with the emissivity uncertainty). Given the general agreement in the magnitude of these estimates and that based on the rms scatter of the measurements of CF itself, we adopt an uncertainty of 12% for the absolute calibration of the 160 μm channel of MIPS.

9.2. Calibration Cross Checks

Soon after the launch of *Spitzer*, observations of a few targets that have well-studied SEDs in the 160 μm region were made, and formed the basis of the initial calibration. These included observations of a few asteroids (those data were included in the analysis above), which led to CF $= 41.6 \pm 8.5$ MJy sr^{-1} MIPS160^{-1}. Observations of K giant calibration stars were affected by the near-IR ghost, but after roughly correcting for the ghost, those data indicated CF $= 37.8 \pm 11.3$ MJy sr^{-1} MIPS160^{-1}. Early science observations of Fomalhaut were also analyzed, and indicated CF $= 39.8 \pm 6.0$ MJy sr^{-1} MIPS160^{-1}. We also analyzed early science data for M33 (Hinz et al. 2004), NGC 55, NGC 2346, and the Marano Strip, which, taken together, indicated CF $= 46.8 \pm 12$ MJy sr^{-1} MIPS160^{-1}. All of these results lead us to adopt an initial calibration for the 160 μm channel of CF $= 42.5 \pm 8.5$ MJy sr^{-1} MIPS160^{-1}. Gordon et al. (2006) have compared MIPS 160 μm measurements of M31 to DIRBE and *ISO* measurements, finding excellent agreement. All of these provide a sanity check of the new calibration, because it is only 1.9% lower than the initial calibration.

More recently, we have compared MIPS measurements of a few ULIRGs to *ISO* measurements of the same objects and to the *IRAS* results for the asteroids observed for the MIPS 160 μm calibration program. In both of these cases we have included comparisons at the shorter MIPS bands, as well as at 160 μm. The comparisons at the shorter wavelengths serve two purposes. Because both the 24 and 70 μm calibrations are entirely based on observations of stars, any short-wavelength spectral leaks present in those channels would bias photometry of cold sources such as ULIRGs and asteroids: the comparisons serve to confirm the lack of such leaks. Because the 160 μm calibration is derived directly from the shorter MIPS bands, the comparisons at those wavelengths also serve to confirm the validity of the 160 μm calibration, even though it (unlike for the shorter bands) is based on observations of red sources.

We reduced *Spitzer* archive data for the ULIRGs IRAS 03538−6432 (5 epochs), IRAS 13536+1836, IRAS 19254−7245, and IRAS 20046−0623 (one epoch for each), and measured their flux densities at 70 and 160 μm. The 70 μm flux densities for the first three were within a few percent of the values we would expect based on the *ISO* photometry reported by Klaas et al. (2001). In particular, for the first two, the MIPS and *ISO* results agreed to better than a percent. The 160 μm flux densities were 5% higher than expected from the *ISO* data, on average. Again, for IRAS 03538−6432 the agreement was within 1%. The MIPS data for IRAS 20046−0623 gave 70 and 160 μm flux densities 25%–30% lower than would be expected from the *ISO* data, but there is no obvious reason for this discrepancy (e.g., no bright background objects that might have fallen within the *ISO* beam).

We have also fitted our 24 and 70 μm observations of asteroids with the STM, deriving diameters for all our targets. The diameters we derive by fitting the two bands independently (for the faint sample) agree quite well: the mean and rms scatter of the ratio of the diameters determined at 24 μm to those determined at 70 μm are 1.02 and 0.051, respectively. This confirms that the calibrations of these two bands are very consistent when applied to observations of red sources. The small deviation of this ratio from unity has a formal significance of 2.8 σ, but could easily be due to the failure of the simple assumptions of the STM to fully describe the thermal emission. We also have compared the diameters determined from our data to the diameters derived from *IRAS* data (the SIMPS catalog; Tedesco et al. 2002). The average and rms scatter of the ratios of the MIPS diameters to the *IRAS* diameters at 24 μm are 1.01 and 0.09, while at 70 μm they are 0.99 and 0.10. We conclude that our calibration in those bands is entirely consistent with the *IRAS* calibration; by inference the 160 μm calibration should also be consistent with *IRAS*.

9.3. Extended Source Calibration

We also checked the calibration on extended sources at 160 μm, using observations of a handful of resolved galaxies that were observed by ISOPHOT using the C_160 broadband filter ($\lambda_{\rm ref} = 170$ μm). The galaxies used for this comparison are M31 (Haas et al. 1998; Gordon et al. 2006), M33 (Hippelein et al. 2003; Hinz et al. 2004), M101 (Stickel et al. 2004; K. D. Gordon et al. 2007, in preparation), as well as NGC 3198, NGC 3938, NGC 6946, and NGC 7793 (Stickel et al. 2004; Dale et al. 2005, 2007). These objects range in diameter from 5′–10′ (the NGC objects) to ≥0.5° (the Messier objects), so they are all highly resolved by both MIPS at 160 μm (40″ FWHM) and ISOPHOT at 170 μm (90″ pixels). We applied color corrections to the MIPS and ISOPHOT measurements and corrected for the difference in wavelengths, assuming the emission has a color temperature of 18 K. The resulting average ratio and uncertainty in the mean of the MIPS 160 μm to ISOPHOT 170 μm flux densities is 0.94 ± 0.06. If the emissivity of the dust in these galaxies is proportional to λ^{-2}, the expected ratio of the measurements is 1.00, consistent to within the uncertainty in the measured mean. Thus, the MIPS and ISOPHOT extended-source calibrations near 160 μm are entirely consistent with one another. These comparisons also indicate that the MIPS point-source-derived calibration at 160 μm is directly applicable to observations of extended sources, and by inference that the aperture corrections in Table 1 are accurate to within a few percent.

9.4. 160 μm Enhanced AOT: Calibration and Sensitivity

In spring 2007 a new 160 μm photometry observing template (the "enhanced AOT") was made available. The goal of the new template is to allow 160 μm photometry data to be time filtered, as has been done all along for the 70 μm data. A limited number of observations (three) taken using the enhanced 160 μm AOT were available at the time of this writing. In each case, the same target was observed using the standard 160 μm AOT as well.

All of these data were reduced in the standard manner, as described earlier. In addition, the enhanced AOT data were processed by applying a high-pass time-domain filter to the time series for each pixel (this filtering process is a standard part of the reduction at 70 μm; Gordon et al. 2005, 2007). Because a dither is performed between all images, the filter preserves the signal from point sources while suppressing elevated noise levels that result from signal drifts in unfiltered data products. Such filtering cannot reliably be applied to data from the standard AOT because the dithers never completely move the source out of the FOV of the array. The result is that time filtering erodes flux from the target source and does so in a way that is flux-dependent. The enhanced AOT implements a wider dither pattern, providing enough data away from the source that the filter works well.

Photometry on the standard AOT, enhanced AOT without time filtering, and enhanced AOT with time filtering was measured as described earlier. We draw preliminary but encouraging conclusions based on these initial results.

1. Photometry measured on the standard and enhanced AOT data agree to within about 5%, except on bright (>1 Jy) sources, where the time-filtered product gives systematically lower fluxes (at about the 10% level). Thus, the enhanced AOT should only be utilized for sources expected to be fainter than about 1 Jy.

2. The time-filtered enhanced AOT data provide significant sensitivity improvements over the standard AOT, unfiltered data. We computed the 1 σ, 500 s noise-equivalent flux density (NEFD; frequently referred to as "sensitivity"). For the old AOT, NEFD = 35 mJy, while for the enhanced AOT, NEFD = 22 mJy. Thus, the enhanced AOT improves the point-source sensitivity of the 160 μm channel by about 35%. We lacked sufficient data to compare the repeatability of the enhanced AOT relative to the old AOT, but expect that it may result in some significant gains, particularly for faint sources and/or higher backgrounds.

10. SUMMARY

We have undertaken a program to calibrate the MIPS 160 μm channel using observations of asteroids. The strategy employed was statistical in nature: rather than perform detailed modeling of a few asteroids to try and accurately predict their 160 μm flux density for our observing circumstances, we instead rely on the average emission properties of asteroids in the spectral range 24–160 μm to allow us to transfer the calibration of our 24 and 70 μm channels to the 160 μm channel. Our 24 and 70 μm data from 51 observations (half of the total; the other 51 did not include 24 μm data) indicate that asteroid spectral energy distributions are indeed all quite similar at these long wavelengths, providing post facto support for the strategy. The calibration factor we derive, which converts the instrumental units of the 160 μm channel (MIPS160) to surface brightness, is 41.7 MJy sr^{-1} MIPS160^{-1}, with a formal uncertainty (uncertainty of the mean) of 0.69 MJy sr^{-1} MIPS160^{-1}. Including the effects of the uncertainties in the 24 and 70 μm calibrations, the observed repeatability of 160 μm measurements of a stellar calibrator and a ULIRG, and allowing for expected uncertainties in aperture and color corrections—and modeling uncertainties—we adopt an uncertainty of 12% on the 160 μm flux determined from an individual measurement of a source. Cross checks of this calibration against those of *ISO* measurements of ULIRGs and nearby galaxies, and against *IRAS* measurements of asteroids, show that the MIPS calibration is quite consistent with those earlier missions.

This work is based on observations made with the *Spitzer Space Telescope*, which is operated by the Jet Propulsion Laboratory, California Institute of Technology, under NASA contract 1407. Support for this work was provided by NASA through contract 1255094 issued by JPL/Caltech. Ephemerides were computed using the services provided by the Solar System Dynamics group at JPL. We thank an anonymous reviewer for input that improved this paper significantly. And we acknowledge the wise insight of Douglas Adams, who pointed out over 20 years ago that the answer *is* 42.

REFERENCES

Beichmann, C. A., et al. 1985, *Infrared Astronomical Satellite* Catalogs and Atlases, Explanatory Supplement, ed. C. A. Beichman et al. (Pasadena: JPL)
Bowell, E., et al. 1989, in Asteroibds II, ed. R. P. Binzel, T. Gehrels, & M. S. Matthews (Tucson: Univ. Arizona Press), 524
Campins, H., et al. 1994, AJ, 108, 2318
Dale, D. A., et al. 2005, ApJ, 633, 857
———. 2007, ApJ, 655, 863
Diolaiti, E., et al. 2000, A&AS, 147, 335
Dole, H., et al. 2006, A&A, 451, 417
Engelbracht, C. W., et al. 2007, PASP, 119, 994
Fazio, G., et al. 2004, ApJS, 154, 10
Fernandez, Y. F., et al. 2002, AJ, 123, 1050
Fixsen, D. J., et al. 1997, ApJ, 490, 482
Gordon, K. D., et al. 2005, PASP, 117, 503
———. 2006, ApJ, 638, L87
———. 2007, PASP, 119, 1019
Haas, M., et al, 1998, A&A, 338, L33
Harris, A. W. 1998, Icarus, 131, 291
Hauser, M. G., et al. 1998, ApJ, 508, 25
Hinz, J. L., et al. 2004, ApJS, 154, 259
Hippelein, H., et al. 2003, A&A, 407, 137
Hora, J. L., et al. 2004, Proc. SPIE, 5487, 77
Houck, J. R., et al. 2004, ApJS, 154, 18
Klaas, U., et al. 2001, A&A, 379, 823
Krist, J. 2002, Tiny Tim/SIRTF User's Guide (Pasadena: SSC)
Lebofsky, L. A., & Spencer, J. R. 1989, in Asteroids II, ed. R. P.Binzel, T. Gehrels, T., & M. S. Matthews (Tucson: Univ. Arizona Press), 128
Lebofsky, L. A., et al. 1986, Icarus, 68, 239
Lumme, K., & Bowell, E. 1981, AJ, 86, 1694
Mather, J. C., et al. 1999, ApJ, 512, 511
Müller, T. G., & Lagerros, J. S. V. 1998, A&A, 338, 340
———. 2002, A&A, 381, 324
Neugebauer, G., et al. 1984, ApJ, 278, L1
Reach, W. T., et al. 2005, PASP, 117, 978
Rieke, G. H., et al. 2004, ApJS, 154, 25
Schulz, B., et al. 2002, A&A, 381, 1110
Stansberry, J. A., et al. 2006, ApJ, 643, 556
Stickel, M., et al. 2004, A&A, 422, 39
Tedesco, E. F., et al. 2002, AJ, 123, 1056
Werner, M. W., et al. 2004, ApJS, 154, 1